



Photonic resonator absorption microscopy: why consider metallic and magneto-plasmonic nano-assemblies over bare nanoparticles for digital biosensing?

Skye Shepherd^{1,3} · Weinan Liu^{1,2} · Seemesh Bhaskar^{1,2,4} · Brian T. Cunningham^{1,2,3,4,5,6}

Received: 26 April 2025 / Revised: 26 July 2025 / Accepted: 29 July 2025
© The Author(s) 2025

Abstract

The unique optical interaction of species such as nanomaterials, proteins, viruses, antibodies, microRNA, and exosomes with the one-dimensional grating-based photonic crystals (PCs) has been leveraged in their detection using photonic crystal absorption microscopy (PRAM). While the principle and fundamental mechanism of such interfacial interactions are well delineated using wavelength and intensity modulations associated with the guided-mode resonance (GMR) of the PC, the effect of nano-assemblies in place of nanoparticles (NPs) has not been reported previously. In this work, the fundamental limitations observed with pristine NPs are overcome through the use of tunable AuNP assemblies synthesized via adiabatic cooling technology, where tunable nano-assemblies are obtained by subjecting the respective NPs to $-196\text{ }^{\circ}\text{C}$. Moreover, the higher contrast rendered by magneto-plasmonic, Fe_3O_4 -Au hybrid nano-assemblies vis-à-vis metallic AuNP assemblies is corroborated with COMSOL Multiphysics simulations using electric and magnetic field hotspots. The high-contrast digital resolution enabled by magneto-plasmonic hybrid nano-assemblies, on account of synergistic coupling between the GMR of the underlying PC, delocalized Bragg, and localized Mie plasmons of dielectric-metal nano-assemblies, demonstrated excellent performance for microRNA-375-3p detection, opening a new window to explore hybrids of tunable “permittivity + permeability” as active probes in the design and development of microscopy-based biosensing modalities.

Keywords Photonic crystal · Enhanced absorption · Magnetic hotspot · Cryosoret · Guided-mode resonance · COMSOL

Published in the topical collection featuring *Optical Imaging Approaches for Biosensing Applications* with guest editors Peter Fechner and Günther Proll.

Skye Shepherd and Weinan Liu contributed equally to this work.

✉ Seemesh Bhaskar
seemeshb@illinois.edu

✉ Brian T. Cunningham
bcunning@illinois.edu

¹ Nick Holonyak Jr. Micro and Nanotechnology Laboratory, University of Illinois at Urbana-Champaign, Urbana, IL 61801, USA

² Department of Electrical and Computer Engineering, University of Illinois at Urbana-Champaign, Urbana, IL 61801, USA

Introduction

Photonic resonator absorption microscopy (PRAM) has emerged as a transformative approach in label-free biosensing, particularly on account of its ability to provide “digital” resolution of individual target molecules with a high signal-to-noise ratio [1–3]. PRAM utilizes photonic crystals (PCs) as a biosensing platform, leveraging their unique optical properties to achieve high-contrast imaging and counting,

³ Department of Bioengineering, University of Illinois at Urbana-Champaign, Urbana, IL 61801, USA

⁴ Carl R. Woese Institute for Genomic Biology, University of Illinois at Urbana-Champaign, Urbana, IL 61801, USA

⁵ Department of Chemistry, University of Illinois at Urbana-Champaign, Urbana, IL 61801, USA

⁶ Cancer Center at Illinois, Urbana, IL 61801, USA

without complex enzymatic amplification and preincubation, which is highly desirable for point-of-care diagnostics [4, 5]. The significance of label-free imaging stems from its ability to detect biomolecular interactions without the need for fluorescent or radioactive labels, offering a more direct and physiologically relevant assessment of biomolecular interactions, including but not limited to molecule-protein, protein-protein, and cell-drug interactions [4]. PCs of various types are well-explored for biosensing applications due to their capability to support several resonances such as Bloch surface wave [6], Fano resonances [7], internal optical modes [8], Fabry-Perot resonances [9], bound states in the continuum (BICs) [10], and guided-mode resonance (GMR) [11, 12], which enhances light-matter interactions and enables highly sensitive detection [13, 14]. Augmented absorption of light at the interface of two systems in a micro-nano-environment has been the topic of interest in areas such as diffraction gratings [15, 16], coherent absorption [17], band nesting [18], and metamaterials [19, 20]. In the past few decades, our group has demonstrated the practical applicability of imaging-based digital counting methods using the GMR effects and enhanced absorption, scattering, and interference of light at the PC interface for detecting individual biomolecular interactions by mapping resonance shifts within a field of view, leading to applications in cancer diagnostics [21–25]. Particularly, PRAM technology has been utilized for the detection of DNA, circulating exosomal microRNA (miRNA), SARS-CoV-2 antigen, specific antibodies, proteins, and enzymes [1, 2, 26–29].

Fundamentally, the operating principle of PRAM relies on the ability of a PC to act as an optical transducer consisting of a periodic arrangement of low and high refractive index materials. When illuminated with broadband light, diffraction causes selective coupling of light into the high-index layer, leading to constructive and destructive interference effects. At a specific resonance condition, nearly all incident light is reflected, producing a sharp optical signal highly sensitive to surface perturbations [30, 31]. The presence of biomolecules or bio-analyte tagged plasmonic nanoparticles (NPs) alters the local refractive index (RI), modifying the peak wavelength value (PWV) and intensity of the reflected light. By mapping these changes, PRAM provides a direct visualization of surface-molecule interactions, cell adhesion, and nanoparticle binding, offering a quantitative and qualitative means for biosensing [4, 30–32]. Despite these advancements, signal contrast rendered by PRAM instrument is limited due to dissimilarities in resonance interactions, particularly when utilizing plasmonic nanomaterials of sharp morphologies as contrast agents [33]. This limitation emerges on account of the intrinsic properties of the plasmonic nanomaterials as their localized surface plasmon resonance (LSPR) is extremely sensitive to the structural morphology (shape), size, composition, as well as the dielectric

constant of the local micro-nano-environment [34, 35]. For instance, nano-urchins that are tagged to bio-analytes function by interacting with the guided-mode resonance of the PC, modulating the resonant wavelength based on changes in local refractive index. However, these nano-urchins that are tuned to match the PC resonance exhibit shifts in LSPR due to deviations in nano-spike morphology [36, 37]. That is, their performance is influenced by variations in their surface topology, as even slight morphological deviations can lead to unintended red or blue shifts in resonance, thereby diminishing detection precision [38–41]. Additionally, we have developed core-shell magneto-plasmonic nano-urchins, which improve detection speed and sensitivity by incorporating magneto-plasmonic effects [2]. While these structures have shown promising results in accelerating assay dynamics, the magnetic core remains embedded within the plasmonic shell, limiting the full exploitation of “magnetic plasmons-PC resonance-EM field” interactions at the biosensor interface. Moreover, surface interactions with analytes sometimes compromise the sharp curvature of nano-urchins, leading to blunting effects that further alter their plasmonic sensing response.

Recently, engineering plasmonic nano-assemblies has emerged with creative solutions to the limitations posed by pristine plasmonic nanomaterials in the domain of imaging and spectroscopic applications [42, 43]. The near-field coupling between the neighboring plasmonic nanomaterials demonstrates nano-gap-based antenna effect which has electric field enhancement effects much greater than those of individual nano-constructs [44–47]. In this context, dimeric, trimeric, tetrameric, octameric, and similarly multimeric core-satellite structures, and nanochains sustaining higher orders of coupled modes have been investigated showcasing interesting concepts from a physics principles perspective as well as applications in dark-field imaging, fluorescence imaging, SPR imaging, and surface-enhanced Raman scattering (SERS) imaging to name a few [43, 44, 47–51]. Among the evolving numerous techniques for the generation of oriented, templated, and directed nano-assembly, template-less, linker-less, and surfactant-free methods based on physical stimuli such as electric field, magnetic field, light-driven, and temperature-dependent approaches have emerged with several advantages as compared to those that are dependent on chemical stimuli (such as pH, ions, acid/base, molecule-triggered nano-assembly) [46, 47]. Among such temperature-stimuli-based self-assembly routes, the cryosoret nano-engineering (CSNE) methodology provides superior optical and plasmonic properties due to collective and coherent resonance effects rendering “hottest hotspots” [52, 53]. Specifically, cryosorets exhibit delocalized Bragg and localized Mie plasmons, making them particularly effective for biosensing applications with applications in single molecule detection and interferometric scattering

microscopy [53, 54]. While interfaced with the PC substrate, the synergistic interplay between resonance modes of PC and cryosorets enhances the signal contrast and its stability, reducing the impact of morphological variations seen in isolated nanoparticles [55]. Additionally, their application in sensing a diverse array of analytes, ranging from ions to small molecules, underscores their versatility and efficacy in high-sensitivity detection platforms.

Moreover, while plasmonic nanomaterials have revolutionized the manipulation of light at the nanoscale, their optical response has predominantly relied on electric field (E-field) interactions due to the absence of intrinsic magnetic moments [56–58]. As such, traditional plasmonic structures, including noble metal nanoparticles, are limited in sustaining magnetic field (H-field) enhancements, particularly within their bulk. To overcome this constraint, recent advances have turned toward high refractive index (HRI) dielectric nanomaterials, which exhibit strong Mie resonances and can simultaneously support E-field and H-field confinement [58–64]. Materials such as Fe_3O_4 offer additional advantages by not only being HRI dielectrics but also exhibiting intrinsic magnetic flux densities. By integrating plasmonic and dielectric components within engineered nano-assemblies, it becomes possible to generate hybrid electromagnetic hotspots—regions of co-localized E-field and H-field enhancement—particularly in nanoscale gaps [2, 65, 66]. These magnetic hotspots introduce a new degree of control over light-matter interactions and can significantly amplify photonic processes such as fluorescence [67, 68]. Motivated by these insights, this study demonstrates a hybrid architecture that synergistically combines Au nanoparticles and Fe_3O_4 nanoparticles within a photonic crystal platform. This approach leverages the dual-field enhancement capabilities to surpass the limitations of previous nano-assemblies, enabling improved signal intensities and spectral control in advanced optical sensing applications.

In this background here, we introduce a novel strategy by synthesizing cryosoret nano-assemblies composed of plasmonic gold (Au) and magnetic iron oxide (Fe_3O_4) nanoparticles, leveraging their combined potential to generate electric and magnetic hotspots. The integration of both materials allows us to exploit unique permittivity-permeability interactions, leading to enhanced optical and EM responses, unlike the conventional hotspots that are only enhancements in the electric field intensity (as in individual metal NPs) [57, 59, 69]. The circulating current densities [70, 71] in these hybrid nano-assemblies generated by three-dimensional nano-gaps further augment contributions from the permeability component of the magnetic Fe_3O_4 NPs [65, 66, 72]. Moreover, by incorporating Fe_3O_4 NPs, the nano-assemblies gain additional unique functionality in the form of tunable magnetic properties, which can be externally manipulated to optimize contrast and signal resolution. This approach

not only improves the signal-to-noise ratio in PRAM but also introduces a new paradigm in nano-assembly design for imaging-based sensing applications. The interplay between localized Mie and delocalized Bragg resonances within the plasmonic-magnetic nano-assemblies [55] presents a compelling avenue for advancing high-contrast imaging with the proof-of-principle for absorption-based precision imaging technology presented in this work.

The hybridization of PRAM with magneto-plasmonic cryosoret nano-assemblies presents a quintessential convergence of PC technology and magneto-plasmonic nano-assemblies at the micro-nano-interface. While our experimental PRAM images present significantly higher contrast for cryosorets vis-à-vis individual nanoparticles, the trend observed for increasing numbers of nanoparticles per assembly is scrutinized both experimentally and using computer-aided COMSOL Multiphysics simulations. Although previous studies have demonstrated the benefits of integrating PCs with nano-assemblies for enhanced sensing applications (spectroscopic and microscopic) [53, 55, 73], our approach uniquely exploits the dual plasmonic and magnetic nature of the hybrid nano-constructs, for the first time to the best of our knowledge. The combination of GMR from PCs with the tunable plasmonic-magnetic interactions of cryosoret nano-assemblies introduces a new approach for digital biosensing that enhances the performance of PRAM beyond conventional limitations mentioned above. This integration enables higher signal contrast, improved analyte-magnetic NP interaction, and greater robustness against environmental fluctuations. Furthermore, the ability to modulate resonance conditions via external magnetic fields offers unprecedented control over biosensing dynamics, paving the way for next-generation label-free imaging platforms. By such interfacial engineering methods, we aim to establish a new standard in photo-plasmonic biosensing, exploiting the fundamental physics of PCs and magneto-plasmonic interactions, using simulation models and experimental methods, to advance the biosensing modalities.

Experiment and simulation

The photonic crystal enhanced absorption (PRAM) is a bio-sensor microscopy platform developed by our team, with details of principle and mechanism of operation presented in earlier works [5, 26, 74]. Briefly, the basic components of the setup include the LED with a range from about 620 to 640 nm that is illuminated onto the PC substrate (from the non-patterned side), using collimating lenses and a polarizer (Fig. 5a). The polarized light is used to excite the specific polarization selective resonance of the PC (transverse magnetic in our case). Typically, in principle, the PC substrate reflects only a narrow band of the LED wavelengths with

approximately 100% reflection efficiency into an uncooled silicon CMOS camera [5, 26]. In the presence of the plasmonic nanomaterial interfaced on the patterned PC substrate, based on the magnitude of absorption rendered by the plasmonic nanomaterial, the reflection intensity changes. Based on this primary concept, our lab has demonstrated the detection of different analytes by using capture ssDNA, toehold—probe on a NP and target analyte such as microRNA, where only in the presence of microRNA the nanoparticle is captured on the PC substrate and individually counted—hence the name “digital detection” [1, 2, 4, 27, 75]. However, this method highly relies on the ability of the nanomaterial to actively function as light absorbing species at the resonance wavelength of the PC. Since the absorption coefficient gets modified (typically hampered) by functionalization with larger sized biomolecules, there is a lookout for alternative approaches to overcome this limitation.

Here, we present the recently developed cryosoret nano-engineering method for achieving this objective. The details of cryosoret engineering method are discussed in our recent works [53, 62, 73, 76]. In brief, the nanoparticles are subjected to $-196\text{ }^{\circ}\text{C}$ by immersing in LN₂ for different time intervals. The thermo-migration induced by the cooling effect results in the generation of nano-assemblies where the adiabatic cooling is overcome by electrostatic repulsion. The synthesized NPs and nano-assemblies were characterized using Asylum Research MFP-3D atomic force microscopy (AFM), Hitachi S-4800 high-resolution scanning electron microscopy (SEM), Au-Pd Sputter Coater—Emscope SC 500, and JEOL 2100 CRYO transmission electron microscopy (TEM).

Thus, obtained NPs and nano-assemblies are later drop-casted over the clean PC substrate and observed under the PRAM optical setup in line with our earlier work [55]. The PC substrate was cleaned using isopropanol, acetone, and deionized water by sonicating for 3 min each, followed by drying using N₂. The drop-casted nanomaterials (nanoparticles and cryosoret nano-assemblies) were incubated on top of the PC substrate in molecular grade water for 1 h at room temperature before imaging using the PRAM instrument [4, 74, 77]. The TEM images of multiple cryosorets (nano-assemblies obtained via cooling nanoparticles to cryo-environment) are used to develop nano-constructs for simulating their optical response in COMSOL Multiphysics software [76].

Sequences

Purchased from Integrated DNA Technologies (Coralville, IA).

Probe-375: CCC ACC TAC ATC ACG CGA GCC GAA CGA ACT TTT TTT TTT TTT TT/3ThioMC3-D/.

Protector-375: GTT CGG CTC GCG TGA TGT AGG.

Capture: TGT AGG TGG GTT TTT TTT TTT TTT TTT TTT/3AmMO/.

Target (miR-375): rUrUrUrGrUrUrCrGrUrUrCrGrGrCrUrCrGr rCrGrUrGrA.

Probe DNA reduction and protector annealing

The thiolated probe was reduced using Tris(2-carboxyethyl)phosphine (TCEP) hydrochloride purchased from Sigma-Aldrich (C4706-2G). Four hundred fifty microliters of 100 μM of probe DNA was added to 50 μL of 50 mM TCEP solution and reduced for 2 h at room temperature. The excess TCEP and byproducts were removed by using 0.5 mL 3 kDa MW Amicon Ultra Centrifugal Filters (Millipore, UFC500308) by centrifuging for 15 min at 14.0 k rcf twice, then washing with 400 μL of molecular grade water. The reduced and concentrated probe was recovered by flipping the filter and centrifuging at 3.0 k rcf for 4 min. The final probe concentration was tested using a NanoDrop One (ThermoScientific), then was diluted in $1\times\text{TE}$ to 100 μM . The protector and thiolated probe sequences were then annealed at a 1:1.5 ratio with the protector in excess in a $1\times\text{TE}$, 12.5 mM MgCl_2 solution by heating to $85\text{ }^{\circ}\text{C}$ then cooling to room temperature. The reduced probe-protector duplex was used immediately for nanoparticle conjugation or was stored at $-20\text{ }^{\circ}\text{C}$ for later use.

Nanoparticle conjugation and cryosoret formation

Twenty milliliters of 20-nm-diameter small gold nanoparticles was incubated with 100 μL of 100 μM of the reduced thiolated probe-protector duplex for 48 h at room temperature in $1\times\text{TE}$, 5 mM MgCl_2 . The AuNPs were then centrifuged three times at 10 k rcf for 30 min to remove unattached probe-protector, and were resuspended in 10 mL $1\times\text{TE}$, 5 mM MgCl_2 for cryosoret formation. Cryosorets were then formed using the pre-functionalized AuNPs and 20-nm magnetic nanoparticles for AuMCS4 (as this variant yielded the highest contrast in the PRAM studies). DNA-functionalized cryosoret assemblies were stored for up to 3 weeks at $4\text{ }^{\circ}\text{C}$.

Surface functionalization of PCs and DNA capture attachment

Photonic crystal chips (1.2 by 1 cm) were glued to coverslips using UV-curable glue (Norland Optical Adhesives 63). The PCs were washed by sonicating for 2 min in acetone, then isopropanol, and then MilliQ® water. PCs were dried using nitrogen gas and heated to $80\text{ }^{\circ}\text{C}$ for 20 min to dry completely. The PCs were oxygen plasma-treated using a PicoDiener machine at 100% power and 0.1 mbar, then were added to a 2% APTES solution in tetrahydrofuran (THF) for 1 h and shaken at 400 rpm at room temperature. Excess

unbound silane was removed by sonicating for 2 min each in THF, acetone, and MilliQ® water. Thin cured polydimethylsiloxane (PDMS) was cut to create six 20- μ L wells, attached to the PC surface using pressure to create separate sample wells. A solution of 100 mM N,N'-disuccinimidyl carbonate (Sigma-Aldrich) in 10% dimethyl sulfoxide (DMSO) was added for 30 min at room temperature, and then excess DSC was removed using three washes of 1% DMSO. The amino-functionalized capture DNA sequence was then reacted with a 50- μ M concentration of capture in water with the DSC-functionalized surface for 3 h at room temperature. Excess capture was removed through washing the surface five times with $1 \times$ TE, Tween20. Finally, the PC surface was blocked for 30 min using PBS SuperBlock (Invitrogen, #37,515). PCs were then immediately used for the PRAM-cryosoret assay.

Detection of miR375 using PRAM-cryosoret assay

Reagents were added into a 20- μ L reaction volume. The assay tested varying concentrations of miR-375 in a five-fold serial dilution (0 fM, 0.8 fM, 4 fM, 20 fM, 100 fM, and 500 fM). The probe-protector cryosorets were added into the well at a final concentration of 1 OD, in $1 \times$ TE, 5 mM MgCl₂, along with the target miR-375. These were allowed to react for 30 min before imaging. Three images were taken per well for each target concentration, and the assay for each concentration was repeated in triplicate. Images were

processed using code previously detailed in [54, 73, 74] with a maximally stable external regions (MSER)-based counting method.

Results and discussion

We start by presenting the comprehensive characterization of the substrate and nanomaterials used for the experimentation. The substrate is a grating-based one-dimensional photonic crystal (PC) that has a sub-wavelength nano-structure with a periodic arrangement of a low refractive index material (silica) coated with a high refractive index (HRI) material (titania). The atomic force microscopy (AFM) image of the PC under investigation is presented in Fig. 1a, with a height profile along the white line shown in Fig. 1b. This, along with the three-dimensional view of the PC shown in Fig. 1c, presents topographical information of the grating interface (with the depth of the grooves being ~ 90 nm). Moreover, the low-resolution scanning electron microscopy (SEM) image shown in Fig. 1d presents the top view confirming the high uniformity of the grating morphology.

The dispersion diagram of the optically active substrate such as metallic thin films, metal-dielectric-metal (MDM) interfaces, and PC presents the transmittance or reflectance response at various wavelengths and angles [78–80]. The dispersion diagram for the PC in this work is shown in Fig. 1e, presenting characteristic guided-mode resonance

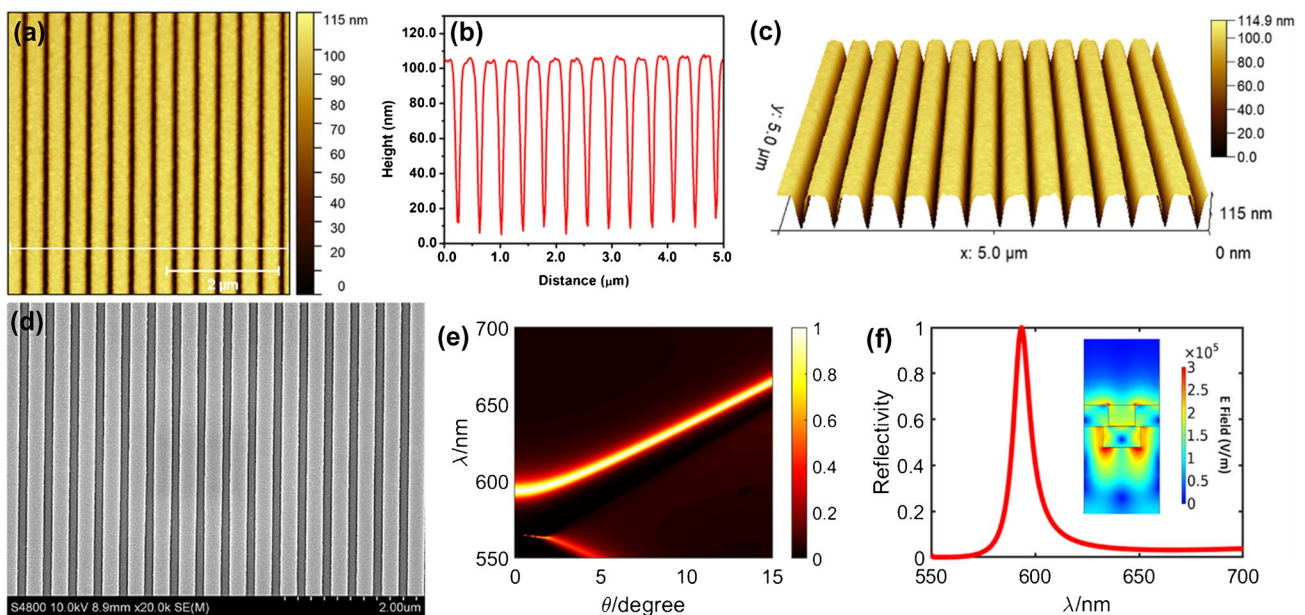


Fig. 1 Structural, morphological, and field distribution of photonic crystal substrate. **a** AFM image showing white light along which the height information is extracted and plotted in **b**. **c** Three-dimensional topographical image of the AFM data shown in **a**. **d** SEM image

showing the top view of the PC substrate. **e** Simulated wavelength vs. angle dispersion diagram of the PC substrate. **f** Simulated reflectance data of the PC substrate obtained at 0° for TM polarization shown with the inset capturing the hotspot E-field intensity distribution

(GMR) modes that arise due to the presence of guiding layer and diffraction elements [81, 82]. The diffracted and guided modes generated upon illumination of white light result in coupling of light into and out of the HRI material, as a consequence of which the destructive interference occurs at zeroth-order transmitted light, resulting in nearly 100% reflection efficiency [11, 83]. The optical response of such PC for all the angles from 0 to 30° under white light illumination is presented in our recent work [62]. It is under this specific wavelength of resonance (GMR) the evanescent field is generated on the top surface of the grating, extending to ~100 nm out of the grating PC substrate. The simulated transmittance dip is shown in Fig. 1f, with the inset presenting the E-field intensity distribution, showing the hotspots at the sharp tips of the grating PC (electric field standing waves).

Interfacing a nano-object at this grating interface at the excitation of GMR of the PC results in optical interaction of such nano-object with the evanescent field generated at resonance. This optical interaction can alter the original intrinsic scattering and absorption effects of the PC and nano-object, which results in either enhanced/quenched scattering and/or absorption. While the photonic crystal interferometric scattering microscopy (PRISM) technology developed by our group heavily relies on the scattering efficiency of the nano-objects [84–86], the photonic resonator absorption microscopy (PRAM) is based on the absorption efficiency of nano-objects, where the interactions render an image in the CCD camera due to resonant optical coupling [1, 2, 87]. Although our earlier works demonstrated substantial changes in near-field distributions, resonant wavelength maximum, and the intensity of the resonant peak (transmittance dip) for interfacing different types of nanomaterials including metallic (AuNPs) and dielectric (TiO₂) [4], all such studies have been limited to a specific size of the nanomaterial. Variations in the size would shift the resonant absorption peak of NPs, thereby resulting in hampered coupling effects. To overcome such drawbacks, we demonstrate the utility of nano-assembly made up of pristine plasmonic gold cryosoret (CS) nano-assemblies and hybrid gold-magnetic cryosorets (MCS) nano-assemblies.

The cryosoret nano-engineering methodology is presented in Fig. 2a conceptually, where the homogenous solution of plasmonic AuNPs subjected to adiabatic cooling results in the generation of gold cryosoret nano-assemblies. A representative 3D simulation of AuCS on glass and PC shown in Fig. 2b clearly indicates the increase in field intensity observed for the AuCS-PC interface. The absorbance spectra of pristine AuNPs show a characteristic LSPR at ~530 nm. The CSs 1–5 are obtained by cooling the AuNP solution to –196 °C at 15 s, 30 s, 1 min, 2 min, and 3 min, respectively [53, 62, 76]. We observe a gradual broadening of the transverse LSPR mode and simultaneous

occurrence of longitudinal modes at higher wavelengths, which are attributed to the generation of anisotropic chain-like nano-assemblies with delocalized Bragg plasmons, in accordance with earlier works [53–55]. Further, the TEM image of pristine AuNPs is shown in Fig. 2d, and Fig. 2e–i presents the TEM images of CSs of gold, presenting an increasing number of AuNPs per assembly. While representative images are presented here, multiple TEM images for each variant are extensively characterized and reported in earlier works [53, 62, 76]. The HRTEM images of representative cryosorets presented in Fig. 2j, k, l show the occurrence of multiple nano-gaps in and around the cryosoret nano-assembly. Such nano-gaps generate gap-induced Bragg scattering modes that results in the observation of spectral broadening as well as longitudinal modes. In this work, we have specifically chosen the AuNPs that show absorbance maximum at values far lower than that of the GMR of the PC to confirm our understanding of resonance coupling. Basically, we aim to validate that even if the nanomaterial does not have LSPR mode at PC resonance, assembling them would yield nanostructures that would be beneficial for digital resolution-based PRAM. That is, if larger size AuNPs are chosen, then there would be non-negligible absorption at the resonance of PC (~630 nm), hence increasing the probability of absorption-induced quenching of PC resonance. The AuNPs chosen here, of size ~20 nm, yield negligible absorption at the PC resonance wavelength, hence serving as an ideal candidate to verify our original hypothesis.

Harnessing the full potential of nanophotonics and magnetism requires careful convergence of associated complementary material platforms. Plasmonic and magnetic nanostructures have each carved distinct but influential trajectories in optical sensing, imaging, and modulation [65, 72, 88]. Yet, it is the hybridization of these two domains—plasmonics and magnetism—that offers a transformative leap, revealing synergistic functionalities that neither system could achieve by themselves. Applications pertaining to plasmonic NPs emerge on account of their ability to support LSPR, which is collective oscillations of conduction electrons that confine light into sub-wavelength regimes [89, 90]. This effect generates intense local electric fields, enabling dramatic enhancements in optical absorption, fluorescence, and Raman scattering. As such, they have been central to the evolution of ultrasensitive biosensors, photothermal therapies, and optical antennas. On the other hand, magnetic nanoparticles (MNPs), like Fe₃O₄, provide a dynamic modality: the ability to respond to external magnetic fields for actuation, spatial control, or signal modulation. Moreover, magnetic nanostructures exhibit magneto-optical (MO) effects such as the Faraday and Kerr effects, which arise due to their non-zero off-diagonal dielectric permittivity components, and such effects have been central to technologies

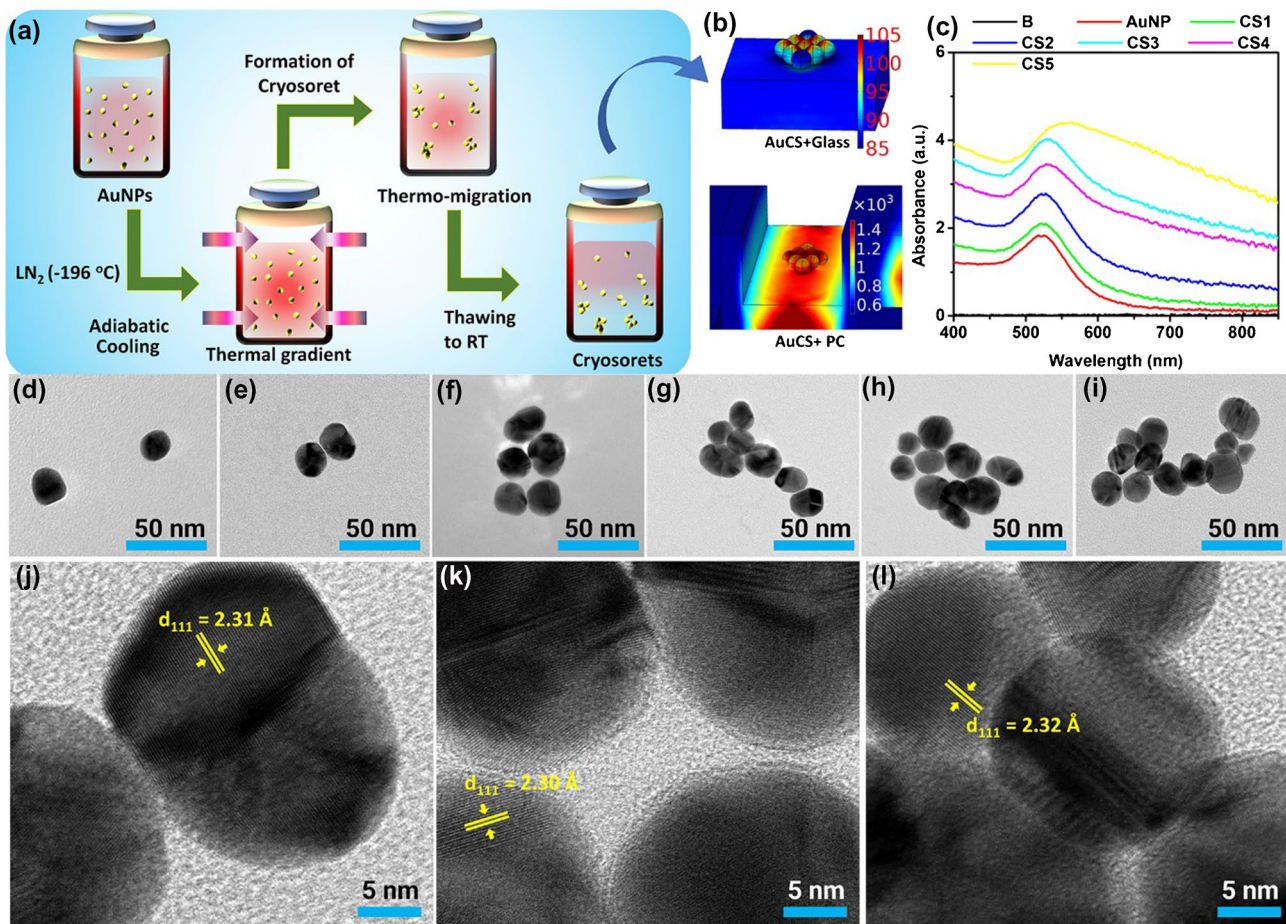


Fig. 2 Synthesis, optical, and electron microscopy characterization of gold cryosorets. **a** Cryosoret nano-engineering method showcasing the steps involved in the generation of AuCSs. **b** Representative simulation of AuCS on glass and PC substrate. **c** Absorbance spectra of all the synthesized gold CSs. **d–i** TEM images of gold CSs [1–5] where the numbers 1–5 represent the samples cooled at 15 s, 30 s, 1 min, 2 min, and 3 min, respectively. High-resolution TEM (HRTEM) images are shown in **j**, **k**, and **l** corresponding to **e**, **f**, and **g**, respectively

involving non-reciprocal light propagation, magnetic field sensing, and active optical switching [65, 72, 88].

It is important to note that despite their individual merits, each system suffers from intrinsic limitations. Magnetic nanomaterials tend to be optically lossy due to suppressed plasmonic resonances. Conversely, while noble metals support strong plasmonic effects, they exhibit weak magneto-optical responses [91, 92]. This dichotomy has spurred intense research into the synthesis and application of magneto-plasmonic nano-constructs, wherein magnetic and plasmonic components are either spatially juxtaposed (as multi-layers for instance) or co-integrated into single hybrid nano-constructs. Such combinations allow external magnetic fields to modulate plasmonic behavior and vice versa, paving the way for tunable sensors, direction-sensitive optics, and enhanced MO signals through field confinement.

In this background, we present a new class of linker-less hybrid nano-assemblies composed of AuNPs and Fe₃O₄

TEM images of gold CSs [1–5] where the numbers 1–5 represent the samples cooled at 15 s, 30 s, 1 min, 2 min, and 3 min, respectively. High-resolution TEM (HRTEM) images are shown in **j**, **k**, and **l** corresponding to **e**, **f**, and **g**, respectively

magnetic NPs with the synthesis method shown in Fig. 3a. A homogenous mixture of AuNPs and Fe₃O₄ NPs was mixed in a 1:1 ratio and subjected to the adiabatic cooling method [52, 54, 62]. The enhanced field coupling between the magneto-plasmonic cryosorets (MCSs) and the PC, as compared to glass, is shown for a representative case in Fig. 3b. Absorbance spectra of all the synthesized MCSs [1–5] are presented in Fig. 3c, where a red-shift in the LSPR of the pristine AuNPs is observed with broadening of the spectra observed for an increasing number of NPs per assembly. Furthermore, the TEM images of the MCS [1–5] are shown in Fig. 3d–h, clearly indicating the anisotropic arrangement of plasmonic AuNPs and Fe₃O₄ NPs in the formation of hybrid cryosorets presenting three-dimensionally distributed hotspots. Also, a few representative HRTEM images are presented along with the lattice fringes characterizing the plasmonic Au (Inorganic Crystal Structure Database, ICSD reference code: 98–061–1625) and dielectric Fe₃O₄ NPs (ICSD reference

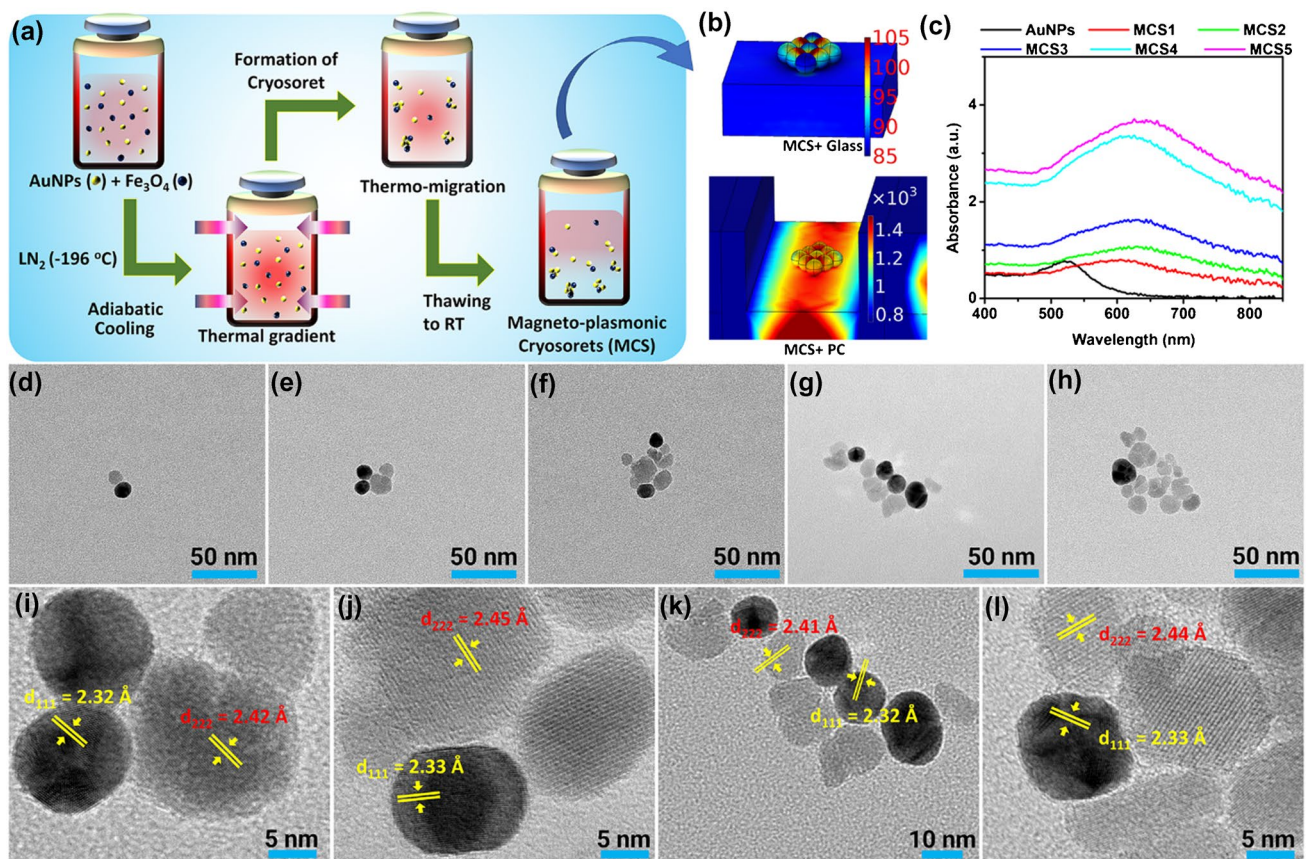


Fig. 3 Synthesis, optical, and electron microscopy characterization of magneto-plasmonic hybrid cryosorets. **a** Cryosoret nano-engineering method showcasing the steps involved in the generation of MCSs. **b** Representative simulation of MCS over glass and PC substrate. **c** Absorbance spectra of all the synthesized MCSs. **d–h** TEM images

of MCSs [1–5] where the numbers 1–5 represent the samples cooled at 15 s, 30 s, 1 min, 2 min, and 3 min, respectively. High-resolution TEM (HRTEM) images are shown in **i**, **j**, **k**, and **l** corresponding to **e**, **f**, **g**, and **h**, respectively

code: 98–008–5807). The high metallic and dielectric nature of the Au and Fe_3O_4 comprising the nano-assemblies are vividly seen due to high and marginal scattering of the electron beam in TEM measurements, rendering the former with dark black and the latter with a light gray color. These well-characterized nanomaterials are further used to build representative models in COMSOL Multiphysics software to comprehend the effect of such multi-particle arrangement in modulating the local E- and H-field intensities.

The study of EM field interactions at the micro-nanoscale remains a cornerstone in advancing plasmonic and magneto-plasmonic explorations. Although the LSPR in metal NPs concentrates electric fields (E-fields) into sub-wavelength volumes, creating E-field hotspots that dramatically enhance light-matter interaction, the magnetic component of light (H-field) is typically weak in conventional plasmonic systems due to the low magnetic permeability at optical frequencies [59, 88, 93]. Recent studies in magneto-plasmonic nanoarchitectures have opened new avenues to co-localize and amplify both E-field and H-field intensities, enabling

applications in enhanced spectroscopy, active photonic devices, and biosensing platforms. In this perspective, several works have reported the tactical use of such hybrid assemblies to achieve tailored field distributions. Maksym et al. reviewed the role of magneto-plasmonic nanoantennas, demonstrating ferromagnetic and plasmonic constituents enabling enhanced magneto-optical effects and dual-mode control of light via E-field and H-field hotspots [94]. Luong et al. investigated Ag-Co composite nanostructures and noted that Faraday rotation could be maximized at the LSPR wavelength, which is a direct consequence of intense E-field concentration and H-field enhancement coexisting in a composite structure [95]. Moreover, the ability of DNA-origami-based magnetic NP rings to simultaneously sustain E-field and H-field dipolar resonances producing tunable magnetic Fano resonances and SPPs in structured networks was reported by Wang et al. [64].

While earlier reports establish the generation of E-field and H-field local enhancement with engineered configurations, interfacing magneto-plasmonic nano-assemblies near

optically active substrates such as PCs is of particular interest as the substrate can further boost the local field intensities through constructive interference and energy funnelling into the existing hottest hotspots [53, 96]. In light of these observations, we performed COMSOL Multiphysics simulations to explore the interplay between NP composition and substrate effects on local field enhancement. As presented in Fig. 4, we modelled the E-field and H-field distributions for both pristine plasmonic gold CSs (based on Au NPs only) and magneto-plasmonic assemblies (Au + Fe₃O₄ NPs, written as MCSs) under transverse magnetic (TM) polarization. In this figure, the continuous black line drawn structures are AuNPs and dotted white line structures are Fe₃O₄ NPs, with the multi-particle arrangement of NPs in the nano-assembly considered as a representative case (as the structural arrangement in the CSs and MCS are anisotropic as seen in TEM images). Simulations were carried out for two substrate conditions: a standard glass substrate and a 1D PC grating engineered to support GMR at the excitation wavelength.

The results from simulations demonstrate a marked enhancement of both E-field and H-field intensities in the MCSs as compared to pristine plasmonic systems (CSs). In spite of its less plasmonic activity, the inclusion of Fe₃O₄ introduces additional pathways for field concentration via magnetic dipole resonances and field confinement at

the NP junctions [97]. This is particularly prominent in the inter-particle gaps and at the periphery of the hybrid assemblies, where co-localized E- and H-hotspots emerge [57, 70, 98]. Moreover, we observed a significant amplification of both field components when the nano-assemblies are placed on the PC substrate rather than glass. We also noted that while E-field enhancement was around an order of magnitude on PC (vis-à-vis glass), the H-field enhancement was around two orders of magnitude higher. This is because the PC acts as a resonant optical cavity, enhancing the interaction between the incident light and the NPs that constitute the nano-assembly. This substrate-induced resonance leads to localized hybrid modes, which are a combination of the GMR of the PC and the LSPR of the NPs, hence culminating in synergistic E- and H-field hotspots with a magnitude of peak intensities higher than on glass.

These observations reinforce the emerging paradigm of PC substrate-driven hybrid E- and H-field hotspots, where material composition and optical confinement may be co-engineered to manipulate optical effects at the nanodimensions. The simultaneous enhancement of E- and H-fields within the same nanoscale region is hence expected to yield intriguing results when observed under the PRAM optical setup, with results presented in Fig. 5.

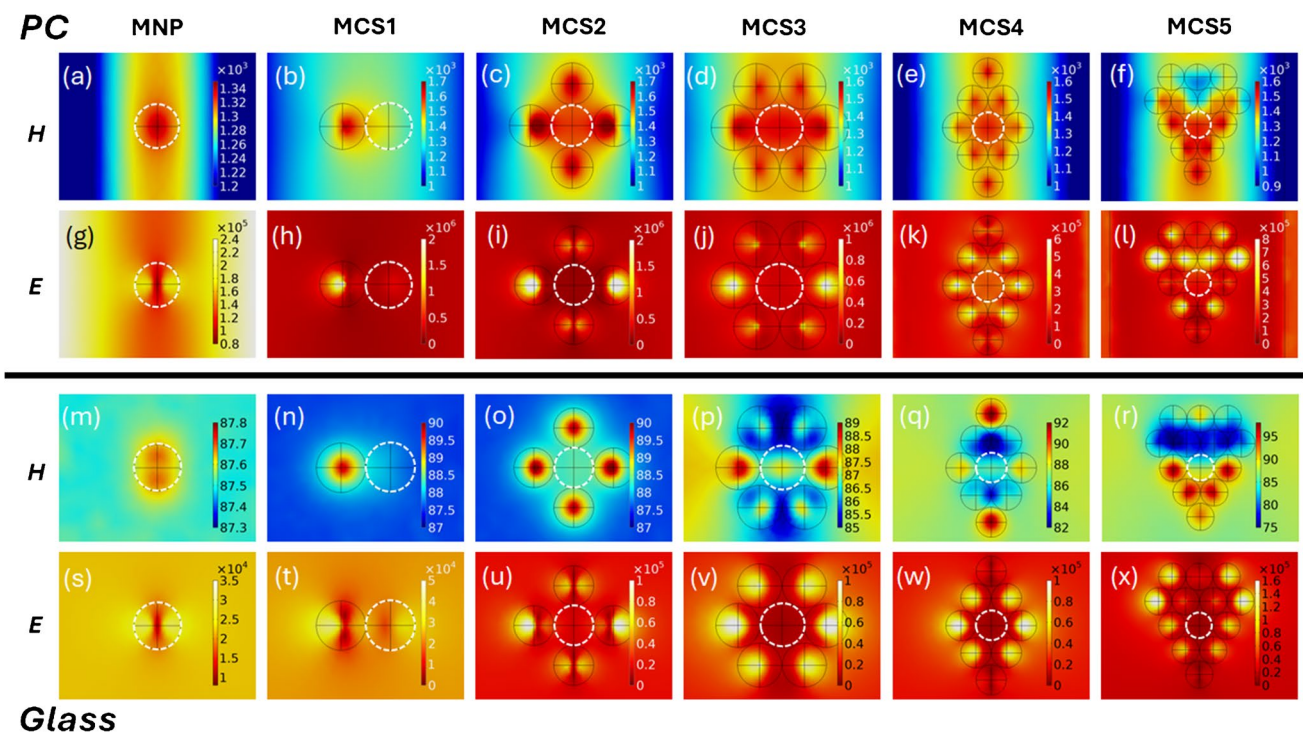


Fig. 4 E-field and H-field distributions of plasmonic CSs and magneto-plasmonic CSs (MCSs). **a–f** H-field and **g–l** E-field intensity distribution of magnetic NP and MCSs 1–5, with the simulations performed over the PC substrate. **m–r** H-field and **s–x** E-field intensity

distribution of magnetic NP and MCSs 1–5, with the simulations performed over the glass substrate. The dotted white line indicates magnetic Fe₃O₄ NP and the continuous black line represents plasmonic AuNP

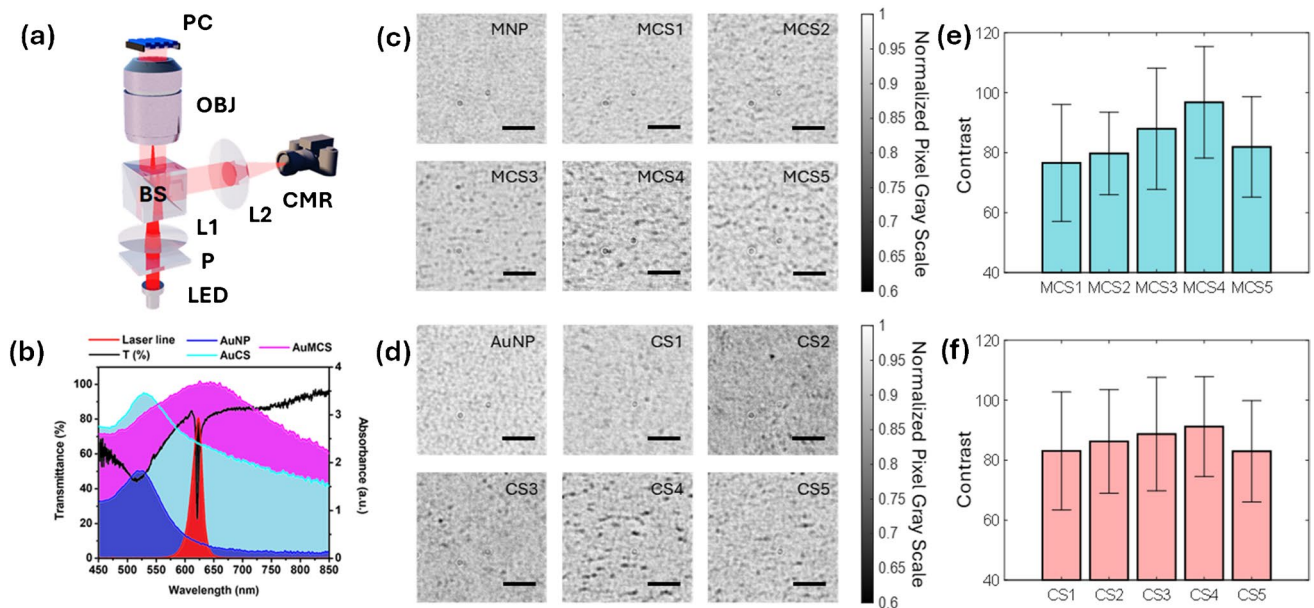


Fig. 5 Photonic crystal absorption microscopy, optical coupling, and contrast analysis. **a** PRAM optical setup comprising LED, polarizer (P), lenses (L1, L2), beam splitter, objective, and camera. **b** Overlap of absorbance spectra of AuNP, AuCS, and AuMCS with the trans-

mittance data of the PC and laser line used. PRAM images of **c** MNCs [1–5] and **d** CSs [1–5]. The scale bar in **c** and **d** is 20 μm. PRAM contrast analysis of **e** MNCs [1–5] and **f** CSs [1–5]

The conceptual schematic of the optical setup used in the PRAM measurements is shown in Fig. 5a, with details presented in the “[Experiment and simulation](#)” section. The absorbance spectra of AuNPs, AuCS, and AuMCS are overlapped with the transmittance dip of the PC and the laser line spectra, all obtained experimentally. The AuCS and AuMCS are chosen for sample variants CS4 and MCS4 from Figs. 2c and 3c, respectively. We have chosen these for representation here because these variants yielded the highest contrast in each of their categories (discussed in the following paragraphs). From Fig. 5b, we note that there is an excellent overlap between the transmittance spectra of the PC resonance and the laser line under TM polarization. Furthermore, the absorption coefficient of AuNPs peaks at ~520 nm and decreases for higher wavelengths, showing almost negligible absorption at the resonance of the PC/laser line. Further, while the AuCS4 presents an increase in the absorption coefficient at higher wavelengths close to PC resonance, a red-shift is observed for AuMCS4, showing an excellent overlap of its plasmon resonance with that of the PC resonance. It is important to note that combining plasmonic and magnetic nanostructures has led to the emergence of novel physical phenomena such as magneto-plasmon-enhanced Faraday rotation, magnetic-field-induced Fano resonances, magnetic SPPs, and artificial magnetic metamaterials exhibiting negative permeability [65, 72, 88]. Although applications have rapidly expanded into multifunctional biosensors, magneto-optical modulators, light-controlled actuators, and

theranostic platforms, the optical contrast response of magneto-plasmonic cryosorets on a PC interface is not reported.

We calculated the signal intensity through a two-step computation of the average contrast of each dark spot generated by the bound NPs or cryosorets. First, the signal spots were recognized with our PRAM image processing algorithm [1, 3, 5, 26]. The algorithm utilized area, pixel intensity, roundness, and Euler number of each spot as factors to screen the signal from non-nanoparticle features in accordance with our earlier works [5]. Due to the spectral misalignment of the LSPR of AuNP, MNP, and the PC’s GMR, there is not a dark spot whose pixel intensity exceeds the algorithm threshold in the 20-nm MNP and AuNP images; hence, no NPs are recognized, as shown in Fig. 5c and d. Second, the contrast was calculated through subtracting the maximum intensity in the image (mean value of the brightest 1000 pixels) from the mean intensity of pixels within the nanoparticle spot (consists of hundreds of pixels). The result is shown in Fig. 5e, f. Figure 5c shows representative cropped PRAM images (FOV: $80 \times 80 \mu\text{m}^2$) for Fe_3O_4 -involved MCSs. Through the calculation, we observed a growing contrast of MCS1–4 as the number of NPs per assembly increased; however, the contrast dropped when more NPs were further aggregated, as shown in Fig. 5e. We attributed this phenomenon to the less dwindled coupling effects between the oversized MCS5 as compared to MCS4, as particle sizes much higher than an optimum limit would render unfavorable optical effects with the evanescent field coupling.

Additionally, the nano-assembly of more NPs demonstrates a larger absorption cross-section, thereby increasing the likelihood of overlapping between adjacent nano-assemblies, and hence resulting in fewer particles being exposed to the illumination and decreased effective absorption. The same phenomenon was also observed in the cryosorets consisting of AuNPs only, as shown in Fig. 5d and f. At this juncture, it is worth noting that the trend observed here, with an initial increase and further decrease in the signal contrast, is in line with our speculations from earlier experimentation of nano-assemblies in interferometric scattering microscopy [55], surface plasmo-coupled emission (SPCE) [53], and photonic crystal-coupled emission (PCCE) experimental measurements [62, 76].

Visualizing the photo-plasmonic effects at the surface of PC following the laser beam presents intriguing inferences. Firstly, the laser beam is incident on the PC surface via a polarizer (Fig. 5a). As the PC is engineered to generate a standing wave with high surface field intensity at this wavelength of laser line and polarization (TM), the PC is set to show GMR with a sharp dip in the transmittance (Fig. 5b) upon illumination. When the nano-assemblies are juxtaposed on the PC under such resonant conditions, the coupling occurs between the GMR of PC and the LSPR of the nanomaterial. The nano-assembly with optimum number of NPs per assembly renders the highest contrast in PRAM. The physical basis for enhanced contrast observed for magneto-plasmonic cryosorets vis-à-vis pristine plasmonic cryosorets is based on the interplay between E- and H-field plasmonic modes discussed in Fig. 4. While AuNPs exhibit strong electric dipolar resonances in the visible regime, Fe₃O₄ contributes magnetic responses that are weak in isolation but can be enhanced via near-field coupling with the plasmonic component. This hybrid configuration allows co-localization of EM hotspots and magnetically active regions, effectively merging optical field enhancement, magnetic effects, and uniform field distribution across the three-dimensional nanogaps of cryosorets.

Unlike conventional molecular absorbers, where extinction arises solely from absorption, nanoparticle-based systems exhibit dual contributions, namely, absorption and scattering, and both of which depend on material and size [99, 100]. In the case of plasmonic NPs, size-dependent plasmonic oscillations can significantly amplify the scattering component [62, 76, 101].

To demonstrate the utility of nanoparticle assemblies on PRAM, DNA-functionalized magneto-plasmonic cryosorets were used in an Activate Capture + Digital Counting assay for miR-375-3p detection. We have used a methodology that has been established and presented with complete details in our earlier works [26]. The AC + DC assay (summarized in Fig. 6a, b) uses toehold-mediated strand displacement reactions to trigger the release of a protector

strand when the complementary target sequence is present, allowing the “activated” probe-functionalized AuMCSs to bind to a capture sequence functionalized on the PC surface to be digitally counted. If no target is present, the protector prevents the AuMCSs from binding. This allows a single target microRNA to activate and capture a cryosoret for PRAM detection. The assay was run for six different miR-375 concentrations in five-fold dilutions spiked into 1xTE, 12.5 mM MgCl₂ buffer. The images were collected after 30 min and counted using image processing, with the details of the sequences and steps involved in the assay presented in the experimental section. Although the limit of detection (LOD) achieved with the cryosoret nano-assemblies in this study (~2.5 fM) is not significantly lower than previously reported values (~160 aM) [26], the approach presented here offers a simpler and more cost-effective alternative, avoiding the need for expensive maleimide-functionalized kits traditionally used for DNA attachment. The reliable performance of the AuMCS in detecting target analytes highlights its potential for multiplexed detection, particularly due to the tunable absorbance spectra achievable with cryosoret nano-assemblies composed of multi-metallic or multifunctional nanomaterials.

Future scope and perspectives

Furthermore, it is informative to present the future scope and perspectives of this research under PRAM imaging setup, especially with regard to the insights that can be drawn by noting the behavior of nano-assemblies on PC substrate. While the isolated NPs remained undetected due to the spectral mismatch between their localized surface plasmon resonance (LSPR) and the guided-mode resonance (GMR) of the PC, the formation of cryosoret nano-assemblies from dimers to higher-order multimers resulted in a pronounced PRAM signal. This contrast enhancement that is absent in single NPs underscores the emergence of inter-particle plasmonic coupling that effectively shifts and broadens the absorption profile of the nano-assemblies into the resonance window of the PC substrate. This observation marks a significant advance over our earlier works (using plasmonic and dielectric NPs of various shapes) and highlights a transformative concept: When a NP exhibits high specificity for a target biomolecule but lacks resonance alignment with the PC, we can circumvent the need for tuning the PC substrate by instead engineering tailored cryosoret nano-assemblies. These nano-assemblies inherently exhibit enhanced absorption at longer wavelengths (longitudinal plasmons), thus bridging the spectral gap and enabling detection without substrate modification. This modular approach can significantly streamline the multiplexing of various analytes on a single chip, which is

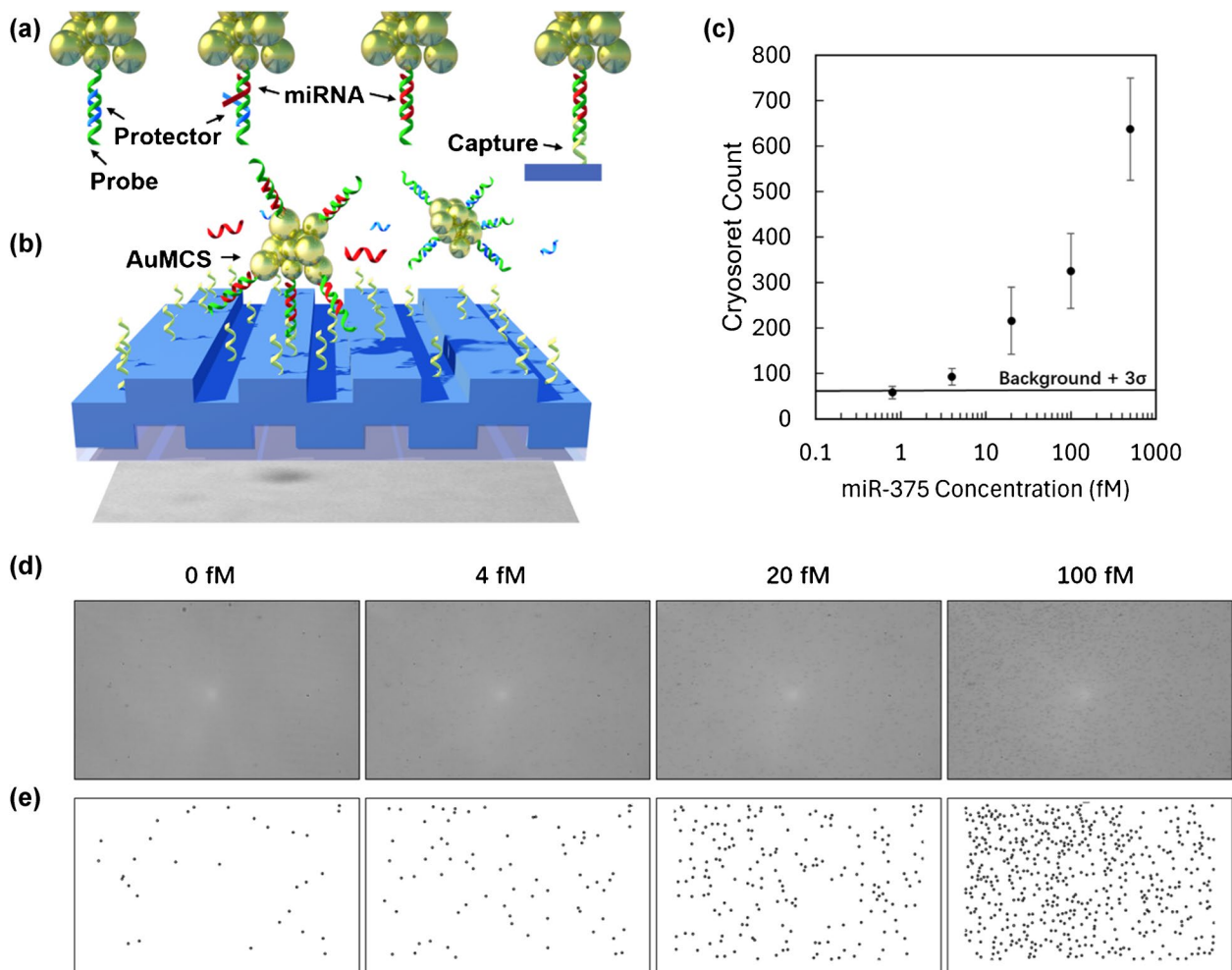


Fig. 6 Assay demonstration of magneto-plasmonic CSs for detection of microRNA-375-3p using PRAM. **a** AC+DC assay using toehold-mediated strand displacement with DNA-functionalized AuMCS. **b** Capture on PC allows digital counting using PRAM. **c** Detection of miR-375 using AuMCS on PRAM, with five-fold serial dilutions

tested ($n=3$). The background is the average of three trials with no miR target plus the standard deviation (black line). **d** Raw PRAM images of four tested concentrations. **e** PRAM-cryosoret images that are processed and counted, with representative dark circles marking particles

otherwise not possible when relying solely on monodisperse, resonance-matched pristine NPs.

Furthermore, the observed nonlinear relationship between the contrast signal and the number of NPs per nano-assembly suggests a complex interplay between EM field localization and scattering losses. Such behavior opens intriguing opportunities for the rational design of NP assemblies that balance field enhancement and absorption cross-section to maximize imaging contrast, the concepts of which have been demonstrated using interferometric scattering effects in our recent report [55]. Future work could involve optimization of assembly geometries (e.g., trimers, tetramers, fractals), material properties (such as metal-dielectric alloys, core-shell, decorated hybrids), and shapes (nanorod, nanourchin, nanostar, nanocubes) to exploit near-field coupling and photo-plasmonic confinement effects. Currently, the

ongoing experiments aim to understand the spectral shifts in terms of peak wavelength and intensity by systematically varying the nanoparticle composition (e.g., Au, Ag, Pt, Pd, Al) and employing hybrid and dielectric materials (e.g., TiO₂, SiO₂). Such shifts, which are governed by modulation of real and imaginary components of the composite dielectric function of the NP-environment system at the resonance wavelength of PC, are expected to offer new routes for finely tuned biosensor responses, especially for label-free detection strategies.

Hence, an exciting frontier lies in the incorporation of magnetic nanomaterials within these plasmonic assemblies to realize magneto-plasmonic cryosorets in three directions: (i) using pristine magnetic NP assemblies, (ii) using hybrid plasmonic + magnetic nano-assemblies, (iii) using dielectric nanoparticles that are doped with certain species to generate

magnetic effects. Such hybrid constructs can enable remote actuation via external magnetic fields, facilitate accelerated bioassay workflows, and allow dynamic manipulation or spatial patterning of sensing elements, which are important features particularly valuable in point-of-care diagnostics. Moreover, the Janus nature of these multifunctional systems could also be harnessed for combined optical and magnetic readouts, unlocking synergistic sensing modalities and novel mechanochemical transduction mechanisms.

Conclusions

The cryosoret nano-assemblies of pristine plasmonic AuNPs and their hybrids with magnetic Fe₃O₄ NPs are synthesized and interfaced on the PC interface and investigated using photonic resonator absorption microscopy (PRAM) as well as using COMSOL Multiphysics simulations. The hybrid coupling between the guided-mode resonance of the underlying PC under TM polarization presented enhanced contrast of the nano-assemblies while their individual counterparts could not be detected. The magneto-plasmonic coupling effects in hybrid cryosorets of plasmonic Au and magnetic Fe₃O₄ NPs presented better contrast as compared to that observed with pristine plasmonic Au-based cryosorets. The simulations presented insights pertaining to such experimental observations where the electric and magnetic flux densities are enhanced for hybrid cryosorets due to the hybrid coupling in magneto-plasmonic nano-assembly. While the isolated metal NPs present electric field hotspots, the emergence of E-field and H-field hotspots in magneto-plasmonic cryosorets over glass interface is established. Additionally, such hotspots are tremendously augmented when the nano-assemblies are interfaced on the PC interface due to the hybridization of delocalized Bragg and localized Mie plasmons of cryosorets with the GMR of the underlying PC substrate.

In summary, the work reported here lays a foundational framework for the use of nano-assemblies on PCs as tunable, high-contrast probes in label-free sensing. Unlike traditional core-shell or layer-by-layer constructs, our assemblies preserve the native surfaces of both NP types. This cryosoret-mediated self-assembly method not only avoids the need for surface linkers, but also ensures that both the magnetic and plasmonic interfaces remain accessible for external functionalization. Such a feature is crucial for biosensing, where nanoparticle surface chemistry dictates specificity and sensitivity. The concept of nano-assembly-mediated resonance bridging introduces a flexible paradigm that could be extended across a variety of PC configurations, including 1D gratings, 2D slab resonators, and 3D colloidal crystal-based PCs (opals

and inverse opals), each offering unique opportunities for enhanced light-matter interactions. Coupling these structures with machine-learning-based design of NP configurations and real-time spectral feedback could lead to adaptive, intelligent biosensors tailored for personalized diagnostics and dynamic opto-fluidic environments. We envisage the development of different types of bioassays (such as sandwich type for example) where the PC substrate is engineered with capture molecules, followed by selective attachment of nano-assembly tagged secondary antibodies, where only in the presence of an analyte the sandwich would manifest, thus enabling highly specific and sensitive multiplexing. Moreover, the simultaneous realization of E-field and H-field intensity distributions in magneto-plasmonic hybrids holds promise for the next-gen integrated biosensors, magneto-optical modulators, and linear-nonlinear hybrid optical devices.

Acknowledgements S.S. thanks the Cancer Center at Illinois for funding. S.B. is supported by a postdoctoral fellowship from the Woese Institute for Genomic Biology. S.B. thanks the research scientists Elbashir Araud, Kathy Walsh, Ying He, Wacek Swiech, Duncan Nall, Umnia Doha, and Glenn Fried for their support and research inputs in characterization of materials. The support from the IGB Core Facilities, instruments including Cypher AFM Asylum, Research WITec Alpha 300 RA Raman-AFM-SNOM and Confocal-Zeiss LSM 710-Multiphoton Microscope, as well as the Cleanroom facility and BioNanotechnology Laboratory (BNL) at HMNTL and the associated research scientists are gratefully acknowledged. The support from the instruments Asylum Research MFP-3D AFM; Hitachi S-4800 High-Resolution SEM; Au-Pd Sputter Coater—Emscope SC 500; and JEOL 2100 CRYO TEM, the associated staff and research scientists at Materials Research Laboratory, the Grainger College of Engineering, UIUC, is gratefully acknowledged. The authors thank the feedback provided by all the members of the Nanosensors group, HMNTL, during scientific discussions.

Author contribution Skye Shepherd: writing—original draft, validation, methodology, investigation, conceptualization. Weinan Liu: writing—original draft, validation, methodology, investigation, software. Seemesh Bhaskar: writing—original draft, validation, methodology, investigation, conceptualization, supervision. Brian T. Cunningham: supervision, writing—review and editing, conceptualization, project administration.

Funding Research was supported by grants from the National Science Foundation (CBET 22-32681) and National Institutes of Health (R33 CA27227).

Data availability The data that support the findings of this study are available from the corresponding authors upon reasonable request.

Declarations

Ethics approval There was no work involving human subjects or animals, and no ethics approval was required.

Conflict of interest BTC is the founder of a company, Atzeyo Biosensors, that is seeking to commercialize PRAM technology. The other authors do not have any conflict of interest.

Open Access This article is licensed under a Creative Commons Attribution 4.0 International License, which permits use, sharing, adaptation, distribution and reproduction in any medium or format, as long as you give appropriate credit to the original author(s) and the source, provide a link to the Creative Commons licence, and indicate if changes were made. The images or other third party material in this article are included in the article's Creative Commons licence, unless indicated otherwise in a credit line to the material. If material is not included in the article's Creative Commons licence and your intended use is not permitted by statutory regulation or exceeds the permitted use, you will need to obtain permission directly from the copyright holder. To view a copy of this licence, visit <http://creativecommons.org/licenses/by/4.0/>.

References

- Canady TD, Li N, Smith LD, Lu Y, Kohli M, Smith AM, et al. Digital-resolution detection of microRNA with single-base selectivity by photonic resonator absorption microscopy. *Proc Natl Acad Sci U S A*. 2019;116(39):19362–7.
- Che C, Xue R, Li N, Gupta P, Wang X, Zhao B, et al. Accelerated digital biodetection using magneto-plasmonic nanoparticle-coupled photonic resonator absorption microscopy. *ACS Nano*. 2022;16(2):2345–54.
- Cunningham BT, Zhuo Y, Harley B, Choi JS, Marin T, Lu Y, inventors; University of Illinois, assignee. Photonic resonator absorption microscopy (PRAM) for digital resolution biomolecular diagnostics patent US11041187B2. 2021.
- Zhuo Y, Hu H, Chen W, Lu M, Tian L, Yu H, et al. Single nanoparticle detection using photonic crystal enhanced microscopy. *Analyst*. 2014;139(5):1007–15.
- Khemtonglang K, Liu W, Lee H, Wang W, Li S, Li ZY, et al. Portable, smartphone-linked, and miniaturized photonic resonator absorption microscope (PRAM mini) for point-of-care diagnostics. *Biomed Opt Express*. 2024;15(10):5691–705.
- Wang R, Xia H, Zhang D, Chen J, Zhu L, Wang Y, et al. Bloch surface waves confined in one dimension with a single polymeric nanofibre. *Nat Commun*. 2017;8(1):14330.
- Liang F, Quan Q. Detecting single gold nanoparticles (1.8 nm) with ultrahigh-Q air-mode photonic crystal nanobeam cavities. *ACS Photonics*. 2015;2(12):1692–7.
- Bhaskar S, Singh AK, Das P, Jana P, Kanvah S, Bhaktha BNS, et al. Superior resonant nanocavities engineering on the photonic crystal-coupled emission platform for the detection of femtomolar iodide and zeptomolar cortisol. *ACS Appl Mater Interfaces*. 2020;12(30):34323–36.
- Zhou J, Xu X, Han W, Mu D, Song H, Meng Y, et al. Fano resonance of nanoparticles embedded in Fabry-perot cavities. *Opt Express*. 2013;21(10):12159–64.
- Xu G, Xing H, Xue Z, Lu D, Fan J, Fan J, et al. Recent advances and perspective of photonic bound states in the continuum. *Ultrafast Sci*. 2023;3:0033.
- Cunningham BT. Biosensing with photonic crystal surfaces. In: 2010 23rd annual meeting of the IEEE photonics society. USA: Denver; 2010. pp. 158–159. <https://doi.org/10.1109/PHOTO NICS.2010.5698806>.
- Cunningham BT, Zhang M, Zhuo Y, Kwon L, Race C. Recent advances in biosensing with photonic crystal surfaces: a review. *IEEE Sens J*. 2016;16(10):3349–66.
- Inan H, Poyraz M, Inci F, A. Lifson M, Baday M, T. Cunningham B, et al. Photonic crystals: emerging biosensors and their promise for point-of-care applications. *Chem Soc Rev*. 2017;46(2):366–88.
- Xiong Y, Shepherd S, Tibbs J, Bacon A, Liu W, Akin LD, et al. Photonic crystal enhanced fluorescence: a review on design strategies and applications. *Micromachines*. 2023;14(3):668.
- Hutley MC, Maystre D. The total absorption of light by a diffraction grating. *Opt Commun*. 1976;19(3):431–6.
- Popov E, Maystre D, McPhedran RC, Nevrière M, Hutley MC, Derrick GH. Total absorption of unpolarized light by crossed gratings. *Opt Express*. 2008;16(9):6146–55.
- Noh H, Chong Y, Stone AD, Cao H. Perfect coupling of light to surface plasmons by coherent absorption. *Phys Rev Lett*. 2012;108(18): 186805.
- Lee S, Seo D, Park SH, Izquierdo N, Lee EH, Younas R, et al. Achieving near-perfect light absorption in atomically thin transition metal dichalcogenides through band nesting. *Nat Commun*. 2023;14(1):3889.
- Landy NI, Sajuyigbe S, Mock JJ, Smith DR, Padilla WJ. Perfect metamaterial absorber. *Phys Rev Lett*. 2008;100(20): 207402.
- Jahani S, Jacob Z. All-dielectric metamaterials. *Nat Nanotechnol*. 2016;11(1):23–36.
- Aguirre Angel M, Long KD, Li N, Manoto SL, Cunningham BT. Detection and digital resolution counting of nanoparticles with optical resonators and applications in biosensing. *Chemosensors*. 2018;6(2): 13.
- Bacon A, Wang W, Lee H, Umrao S, Sinawang PD, Akin D, et al. Review of HIV self testing technologies and promising approaches for the next generation. *Biosensors*. 2023;13(2):298.
- Barya P, Xiong Y, Shepherd S, Gupta R, Akin LD, Tibbs J, et al. Photonic-plasmonic coupling enhanced fluorescence enabling digital-resolution ultrasensitive protein detection. *Small*. 2023;19(44):2207239.
- Bhaskar S, Liu W, Tibbs J, Cunningham BT. Photonic crystal-coupled enhanced steering emission: a prism-free, objective-free, and metal-free loss-less approach for biosensing. *Appl Phys Lett*. 2024;124(16): 161102.
- Ghosh S, Li N, Xiong Y, Ju Y-G, Rathslag MP, Onal EG, et al. A compact photonic resonator absorption microscope for point of care digital resolution nucleic acid molecular diagnostics. *Biomed Opt Express*. 2021;12(8):4637–50.
- Li N, Canady TD, Lu Y, Kohli M, Smith AM, Cunningham BT. Digital detection of microRNA with nanoparticle tags under photonic resonator absorption microscopy. In: Optical sensors and sensing congress, OSA Technical Digest. Optica Publishing Group; 2020. pp. SM4B.2.
- Wang X, Shepherd S, Li N, Che C, Song T, Xiong Y, et al. A target recycling amplification process for the digital detection of exosomal microRNAs through photonic resonator absorption microscopy. *Angew Chem Int Ed Engl*. 2023;62(16): e202217932.
- Zhao B, Wang W, Li N, Garcia-Lezana T, Che C, Wang X, et al. Digital-resolution and highly sensitive detection of multiple exosomal small RNAs by DNA toehold probe-based photonic resonator absorption microscopy. *Talanta*. 2022;241: 123256.
- Chen W, D. Long K, Yu H, Tan Y, Sun Choi J, A. Harley B, et al. Enhanced live cell imaging via photonic crystal enhanced fluorescence microscopy. *Anal*. 2014;139(22):5954–63.
- Shafiee H, Lidstone EA, Jahangir M, Inci F, Hanhauser E, Henrich TJ, et al. Nanostructured optical photonic crystal biosensor for HIV viral load measurement. *Sci Rep*. 2014;4(1):4116.
- Peterson RD, Cunningham BT, Andrade JE. A photonic crystal biosensor assay for ferritin utilizing iron-oxide nanoparticles. *Biosens Bioelectron*. 2014;56:320–7.
- Shao L, Susha AS, Cheung LS, Sau TK, Rogach AL, Wang J. Plasmonic properties of single multispired gold nanostars: correlating modeling with experiments. *Langmuir*. 2012;28(24):8979–84.
- Zhang H, Wang R, Sikdar D, Wu L, Sun J, Gu N, et al. Plasmonic superlattice membranes based on bimetallic nano-sea urchins as

- high-performance label-free surface-enhanced raman spectroscopy platforms. *ACS Sens.* 2022;7(2):622–31.
34. Gao Y, Wang J, Wang W, Zhao T, Cui Y, Liu P, et al. More symmetrical “hot spots” ensure stronger plasmon-enhanced fluorescence: from Au nanorods to nanostars. *Anal Chem.* 2021;93(4):2480–9.
 35. Montaña-Priede JL, Sánchez-Iglesias A, Mezzasalma SA, Sancho-Parramon J, Grzelczak M. Quantifying shape transition in anisotropic plasmonic nanoparticles through geometric inversion. Application to gold bipyramids. *J Phys Chem Lett.* 2024;15(14):3914–22.
 36. Vernier C, Portalès H. Impact of tip curvature and edge rounding on the plasmonic properties of gold nanorods and their silver-coated counterparts. *J Chem Phys.* 2024;161(12).
 37. Delgado-Corrales BJ, Chopra V, Chauhan G. Gold nanostars and nanourchins for enhanced photothermal therapy, bioimaging, and theranostics. *J Mater Chem B.* 2025;13(2):399–428.
 38. Li J, Wu J, Zhang X, Liu Y, Zhou D, Sun H, et al. Controllable synthesis of stable urchin-like gold nanoparticles using hydroquinone to tune the reactivity of gold chloride. *J Phys Chem C.* 2011;115(9):3630–7.
 39. Li Y, Zhai M, Xu H. Controllable synthesis of sea urchin-like gold nanoparticles and their optical characteristics. *Appl Surf Sci.* 2019;498: 143864.
 40. Quang ATN, Nguyen TA, Vu SV, Lo TNH, Park I, Vo KQ. Facile tuning of tip sharpness on gold nanostars by the controlled seed-growth method and coating with a silver shell for detection of thiram using surface enhanced Raman spectroscopy (SERS). *RSC Adv.* 2022;12(35):22815–25.
 41. Ahmed SR, Nagy E, Neethirajan S. Self-assembled star-shaped chiroplasmonic gold nanoparticles for an ultrasensitive chiro-immunosensor for viruses. *RSC Adv.* 2017;7(65):40849–57.
 42. Bhaskar S, Das P, Moronshing M, Rai A, Subramaniam C, Bhaktha SBN, et al. Photoplasmonic assembly of dielectric-metal, Nd2O3-gold soret nanointerfaces for dequenching the lumiphore emission. *Nanophotonics.* 2021;10(13):3417–31.
 43. Boles MA, Engel M, Talapin DV. Self-assembly of colloidal nanocrystals: from intricate structures to functional materials. *Chem Rev.* 2016;116(18):11220–89.
 44. Chakraborty S, Guchhait A, Ong X, Mishra N, Wu W-Y, Jhon MH, et al. Facet to facet linking of shape anisotropic inorganic nanocrystals with site specific and stoichiometric control. *Nano Lett.* 2016;16(10):6431–6.
 45. Deng K, Luo Z, Tan L, Quan Z. Self-assembly of anisotropic nanoparticles into functional superstructures. *Chem Soc Rev.* 2020;49(16):6002–38.
 46. Grzelczak M, Liz-Marzán LM, Klajn R. Stimuli-responsive self-assembly of nanoparticles. *Chem Soc Rev.* 2019;48(5):1342–61.
 47. Grzelczak M, Vermant J, Furst EM, Liz-Marzán LM. Directed self-assembly of nanoparticles. *ACS Nano.* 2010;4(7):3591–605.
 48. Gupta D, Varghese BS, Suresh M, Panwar C, Gupta TK. Nano-architectonics: functional nanomaterials and nanostructures—a review. *J Nanopart Res.* 2022;24(10):196.
 49. Li Z, Fan Q, Yin Y. Colloidal self-assembly approaches to smart nanostructured materials. *Chem Rev.* 2022;122(5):4976–5067.
 50. Rao A, Roy S, Jain V, Pillai PP. Nanoparticle self-assembly: from design principles to complex matter to functional materials. *ACS Appl Mater Inter.* 2023;15(21):25248–74.
 51. Bhaskar S. Biosensing technologies: a focus review on recent advancements in surface plasmon coupled emission. *Micromachines.* 2023;14(3):574.
 52. Rai A, Bhaskar S, Ganesh KM, Ramamurthy SS. Hottest hotspots from the coldest cold: welcome to Nano 4.0. *ACS Appl Nano Mater.* 2022;5(9):12245–64.
 53. Cheerla VSK, Ganesh KM, Bhaskar S, Ramamurthy SS, Neelakantan SC. Smartphone-based attomolar cyanide ion sensing using Au-graphene oxide cryosoret nanoassembly and benzoxazolium-based fluorophore in a surface plasmon-coupled enhanced fluorescence interface. *Langmuir.* 2023;39(22):7939–57.
 54. Liu L, Bhaskar S, Cunningham BT. Hybrid interfacial cryosoret nano-engineering in photonic resonator interferometric scattering microscopy: insights from nanoparticles and nano-assemblies. *Appl Phys Lett.* 2024;124(23): 234101.
 55. Alu A, Engheta N. The quest for magnetic plasmons at optical frequencies. *Opt Express.* 2009;17(7):5723.
 56. Bhaskar S, Srinivasan V, Ramamurthy SS. Nd2O3-Ag nanostructures for plasmonic biosensing, antimicrobial, and anticancer applications. *ACS Appl Nano Mater.* 2023;6(2):1129–45.
 57. Calandrini E, Cerea A, Angelis FD, Zaccaria RP, Toma A. Magnetic hot-spot generation at optical frequencies: from plasmonic metamolecules to all-dielectric nanoclusters. *Nanophotonics.* 2019;8(1):45–62.
 58. Alaeian H, Dionne JA. Plasmon nanoparticle superlattices as optical-frequency magnetic metamaterials. *Opt Express.* 2012;20(14):15781–96.
 59. Baranov DG, Zuev DA, Lepeshov SI, Kotov OV, Krasnok AE, Evlyukhin AB, et al. All-dielectric nanophotonics: the quest for better materials and fabrication techniques. *Optica.* 2017;4(7):814–25.
 60. Barreda Á, Vitale F, Minovich AE, Ronning C, Staude I. Applications of hybrid metal-dielectric nanostructures: state of the art. *Adv Photon Res.* 2022;3(4): 2100286.
 61. Bhaskar S, Liu L, Liu W, Tibbs J, Akin LD, Bacon A, et al. Photonic crystal band edge coupled enhanced fluorescence from magneto-plasmonic cryosoret nano-assemblies for ultra-sensitive detection. *APL Mater.* 2025. <https://doi.org/10.1063/5.0251312>.
 62. Mayer M, Schnepf MJ, König TAF, Fery A. Colloidal self-assembly concepts for plasmonic metasurfaces. *Adv Opt Mater.* 2019;7(1):1800564.
 63. Wang P, Huh J-H, Lee J, Kim K, Park KJ, Lee S, et al. Magnetic plasmon networks programmed by molecular self-assembly. *Adv Mater.* 2019;31(29):1901364.
 64. Maksymov IS. Magneto-plasmonic nanoantennas: basics and applications. *Rev Phys.* 2016;1:36–51.
 65. Nguyen TT, Mameri F, Ammar S. Iron oxide and gold based magneto-plasmonic nanostructures for medical applications: a review. *Nanomaterials.* 2018;8(3): 149.
 66. Takemura K, Lee J, Suzuki T, Hara T, Abe F, Park EY. Ultrasensitive detection of norovirus using a magnetofluoroimmunoassay based on synergic properties of gold/magnetic nanoparticle hybrid nanocomposites and quantum dots. *Sens Actuators, B Chem.* 2019. <https://doi.org/10.1016/j.snb.2019.126672>.
 67. Zhang R, Le B, Xu W, Guo K, Sun X, Su H, et al. Magnetic “squashing” of circulating tumor cells on plasmonic substrates for ultrasensitive NIR fluorescence detection. *Small Methods.* 2019;3(2):1800474.
 68. Sachan R, Malasi A, Ge J, Yadavali S, Krishna H, Gangopadhyay A, et al. Ferroplasmons: intense localized surface plasmons in metal-ferromagnetic nanoparticles. *ACS Nano.* 2014;8(10):9790–8.
 69. Wu Y, Xie P, Ding Q, Li Y, Yue L, Zhang H, et al. Magnetic plasmons in plasmonic nanostructures: an overview. *J Appl Phys.* 2023;133(3): 030902.
 70. Alù A, Engheta N. Dynamical theory of artificial optical magnetism produced by rings of plasmonic nanoparticles. *Phys Rev B.* 2008;78(8): 085112.
 71. Rizal C, Shimizu H, Mejía-Salazar JR. Magneto-optics effects: new trends and future prospects for technological developments. *Magnetochemistry.* 2022;8(9):94.
 72. Cheerla VSK, Ganesh KM, Bhaskar S, Ramamurthy SS, Neelakantan SC. Smartphone-based attomolar cyanide ion

- sensing using Au-graphene oxide cryosoret nanoassembly and benzoxazolium-based fluorophore in a surface plasmon-coupled enhanced fluorescence interface. *Langmuir*. 2023. <https://doi.org/10.1021/acs.langmuir.3c00801>.
73. Liu W, Ayupova T, Wang W, Shepherd S, Wang X, Akin LD, et al. Dynamic and large field of view photonic resonator absorption microscopy for ultrasensitive digital resolution detection of nucleic acid and protein biomarkers. *Biosens Bioelectron*. 2024;264: 116643.
 74. S SML, Bhaskar S, Dahiwardkar R, Kanvah S, Ramamurthy SS, Bhaktha B N S. Plasmon-rich BCZT nanoparticles in the photonic crystal-coupled emission platform for cavity hotspot-driven atomolar sensing. *ACS Appl Nano Mater* 2023;6:19312–26. <https://doi.org/10.1021/acsnm.3c03731>.
 75. Bhaskar S, Liu L, Liu W, Tibbs J, Cunningham BT. Photonic-crystal-enhanced fluorescence: template-free gold cryosoret nanoassembly steering, dequenching, and augmenting the quenched emission from radiating dipoles. *MRS Bull*. 2025.
 76. Zhao B, Che C, Wang W, Li N, Cunningham BT. Single-step, wash-free digital immunoassay for rapid quantitative analysis of serological antibody against SARS-CoV-2 by photonic resonator absorption microscopy. *Talanta*. 2021;225: 122004.
 77. Dutta Choudhury S, Badugu R, Ray K, Lakowicz JR. Steering fluorescence emission with metal-dielectric-metal structures of Au, Ag, and Al. *J Phys Chem C*. 2013;117(30):15798–807.
 78. Gryczynski I, Malicka J, Gryczynski Z, Lakowicz JR. Radiative decay engineering 4. Experimental studies of surface plasmon-coupled directional emission. *Anal Biochem*. 2004;324(2):170–82.
 79. Gryczynski I, Malicka J, Nowaczyk K, Gryczynski Z, Lakowicz JR. Effects of sample thickness on the optical properties of surface plasmon-coupled emission. *J Phys Chem B*. 2004;108(32):12073–83.
 80. Drayton A, Barth I, Krauss TF. Chapter Five - Guided mode resonances and photonic crystals for biosensing and imaging. In: Zhou W, Fan S, editors. *Semiconductors and semimetals*. Elsevier. 2019;100:115–48.
 81. Pitruzzello G, Krauss TF. Photonic crystal resonances for sensing and imaging. *J Opt*. 2018;20(7): 073004.
 82. Chan LL, Cunningham BT, Li PY, Puff D. A self-referencing method for microplate label-free photonic-crystal biosensors. *IEEE Sens J*. 2006;6(6):1551–6.
 83. Li N, Canady TD, Huang Q, Wang X, Fried GA, Cunningham BT. Photonic resonator interferometric scattering microscopy. *Nat Commun*. 2021;12(1):1744.
 84. Li N, Wang X, Tibbs J, Che C, Peinetti AS, Zhao B, et al. Label-free digital detection of intact virions by enhanced scattering microscopy. *J Am Chem Soc*. 2022;144(4):1498–502.
 85. Liu L, Tibbs J, Li N, Bacon A, Shepherd S, Lee H, et al. A photonic resonator interferometric scattering microscope for label-free detection of nanometer-scale objects with digital precision in point-of-use environments. *Biosens Bioelectron*. 2023;228: 115197.
 86. Shepherd S, Liu W, Cunningham BT. Abstract 3676: Ultrasensitive protein detection using proximity initiated nucleic acid target amplification with digital biosensing. *Cancer Res*. 2025;85(8_Supplement_1):3676.
 87. Alù A, Engheta N. The quest for magnetic plasmons at optical frequencies. *Opt Express*. 2009;17(7):5723–30.
 88. Bauch M, Toma K, Toma M, Zhang Q, Dostalek J. Plasmon-enhanced fluorescence biosensors: a review. *Plasmonics*. 2014;9(4):781–99.
 89. Jiang N, Zhuo X, Wang J. Active plasmonics: principles, structures, and applications. *Chem Rev*. 2018;118(6):3054–99.
 90. Tran VT, Kim J, Tufa LT, Oh S, Kwon J, Lee J. Magnetoplasmonic nanomaterials for biosensing/imaging and *in vitro / in vivo* biocompatibility. *Anal Chem*. 2018;90(1):225–39.
 91. Zhou H, Zou F, Koh K, Lee J. Multifunctional magnetoplasmonic nanomaterials and their biomedical applications. *J Biomed Nanotechnol*. 2014;10(10):2921–49.
 92. Bakhti S, Tishchenko AV, Zambrana-Puyalto X, Bonod N, Dhuey SD, Schuck PJ, et al. Fano-like resonance emerging from magnetic and electric plasmon mode coupling in small arrays of gold particles. *Sci Rep*. 2016;6(1):32061.
 93. Maksymov IS. Magneto-plasmonics and resonant interaction of light with dynamic magnetisation in metallic and all-magneto-dielectric nanostructures. *Nanomaterials*. 2015;5(2):577–613.
 94. Luong HM, Pham MT, Ai B, Nguyen TD, Zhao Y. Magnetoplasmonic properties of Ag-Co composite nanohole arrays. *Phys Rev B*. 2019;99(22): 224413.
 95. Kneipp K, Kneipp H, editors. *Surface enhanced Raman scattering using the “hottest” hot spots only*. Photonic Metamaterials and Plasmonics: Optica Publishing Group. 2010.
 96. Liu N, Mukherjee S, Bao K, Brown LV, Dorfmueller J, Nordlander P, et al. Magnetic plasmon formation and propagation in artificial aromatic molecules. *Nano Lett*. 2012;12(1):364–9.
 97. Shafiei F, Monticone F, Le KQ, Liu X-X, Hartsfield T, Alù A, et al. A subwavelength plasmonic metamolecule exhibiting magnetic-based optical Fano resonance. *Nat Nanotechnol*. 2013;8(2):95–9.
 98. Bhaskar S, Wang W, Lee H, Liu L, Umrao S, Liu W, et al. Photonic crystal grating resonance and interfaces for health diagnostic technologies. *Chem Rev*. 2025;125(14):6435–40. <https://doi.org/10.1021/acs.chemrev.4c00653>.
 99. Lakowicz JR, Ray K, Chowdhury M, Szmackinski H, Fu Y, Zhang J, et al. Plasmon-controlled fluorescence: a new paradigm in fluorescence spectroscopy. *Analyst*. 2008;133(10):1308–46.
 100. Lakowicz JR. Radiative decay engineering 5: metal-enhanced fluorescence and plasmon emission. *Anal Biochem*. 2005;337(2):171–94.
 101. Lakowicz JR. Plasmonics in biology and plasmon-controlled fluorescence. *Plasmonics*. 2006;1(1):5–33.

Publisher's Note Springer Nature remains neutral with regard to jurisdictional claims in published maps and institutional affiliations.